Free-template synthesis of porous carbon nanofiber assembled by hollow carbon nanospheres and their adsorption kinetics and isotherms for methylene blue

Tao Ni, Zhigang Jia*, Ziyu Li, Shengbiao Li

School of Chemistry and Chemical Engineering, Anhui University of Technology, No. 59 Hudong Road, Ma'anshan 243002, Anhui Province, China, Tel. + 86-555-2311551; Fax: + 86-555-2311882; emails: zjchemyue@126.com (Z. Jia), 3013261430@qq.com (T. Ni), 496761147@qq.com (Z. Li), 283317835@qq.com (S. Li)

a b s t r a c t

In this work, porous carbon nanofibers assembled by hollow carbon spheres were first obtained via calcination and subsequent acid leaching process for nitrilotriacetic acid nickel salt nanofibers. The as-obtained samples were characterized by various techniques such as scanning electron microscopy, transmission electron microscopy, X-ray diffraction, Fourier transform infrared spectroscopy and N_2 adsorption/desorption measurement. The results showed that the as-prepared carbon nanofibers with higher surface area were built by plenty of Ni(NiO)/carbon composite nanoparticles or hollow carbon nanospheres containing rich active groups. The formation mechanism of porous carbon nanofibers was also discussed. The adsorption performance of the as-prepared carbon fibers for methylene blue (MB), such as the kinetics, isotherms and thermodynamic property, was investigated in detail. The adsorption of samples NC-1 and NC-2 for MB could be fitted to pseudo-second-order model. The Langmuir adsorption model agreed well with the experimental data. Thermodynamic parameters revealed the spontaneity and the endothermic nature of the adsorption process. These results demonstrated that the as-prepared carbon nanofibers can be used for the treatment of dye-containing wastewater.

Keywords: Carbon nanofiber; Composite; Hollow nanosphere; Adsorption

1. Introduction

Dyes are widely used in various industries such as textile, pharmaceutical, leather, paper, printing, cosmetic, etc. It is reported that over 70,000 tons of dye with more than 100,000 kinds are produced annually. Unfortunately, 15%–20% of that production is lost during the dyeing process. The dyes invariably enter the effluents and further contaminate the surrounding water bodies and groundwater [1–3]. Many dyes are inert, toxic and difficult to biodegrade in water bodies. The water containing dyes possesses a potential health hazard to all forms of life [4,5]. Therefore, it is imperative to develop a proper treatment route before discharging them into the environment.

So far, many investigations have been conducted to remove the dye from water bodies. Various means, such as biological treatment [6,7], chemical oxidation [8–10], ozone treatment [11,12], photocatalytic degradation [13,14], coagulation/flocculation [15,16], ion-exchange [17,18] and adsorption [19,20], have been developed to destroy or remove the dyes from wastewater. From an economic and efficiency point of view, adsorption is regarded as one of the most promising and widely used methods.

Carbon nanofibers (CNFs) are of great interest due to their high aspect ratio, large specific surface area, high-temperature resistance and good electrical/thermal conductivities. As adsorbent, carbon fibers have been used to remove the bulky dye molecules and show high adsorption capacity [21–23]. The conventional synthetic strategies for CNFs, including the substrate method, vapor growth

* Corresponding author.

method, spraying method and plasma-enhanced chemical vapor deposition method, are known to be very complicated and costly [24–27]. Therefore, it is still a challenge to seek a new strategy for the preparation of CNFs with good adsorption capacity for dye molecule.

In this study, we reported a novel preparation of CNFs based on nitrilotriacetic acid nickel salt (Ni-NTA) nanofibers, which was first synthesized with NiCl$_2$ and NTA by the hydrothermal method. CNFs decorated with nanoparticles were obtained by calcining Ni-NTA nanofibers precursor under sealed atmosphere. Furthermore, we found that the as-formed CNFs were built by plenty of hollow carbon nanoparticles. This kind of novel structure was favorable for the purpose as adsorbent to remove the pollutant. MB was employed to estimate the adsorption performance of the as-prepared CNFs. The removal kinetics, thermodynamics and isotherms data of the adsorption were evaluated to study the adsorption process of MB molecules onto the prepared carbon fiber aerogels.

2. Experimental section

2.1. Synthesis of Ni-NTA nanofibers

Ni-NTA nanofibers were prepared by a hydrothermal route according to Wang's method with a minor modification [28]. In a typical synthesis, 3 mmol NiCl$_2$ was dissolved into the mixture of isopropanol and water. Then, 3 mmol NTA was added. After thorough stirring, the mixture was transferred into a Teflon lined autoclave and hydrothermally treated at 180°C for 24 h. The resultant light blue floccules were collected by filtration, washed with deionized water and pure ethanol, and air-dried at 100°C.

2.2. Preparation of carbon nanofibers with/without Ni(NiO)

The as-prepared Ni-NTA nanofibers were calcined at 400°C for 2 h under sealed condition. The obtained sample was denoted as NC-1. The as-prepared NC-1 was then immersed into the HCl (2.0 M, 40 mL) with stirring overnight. The immersed sample (denoted as NC-2) was collected by filtration and washed with distilled water several times until the filtrate was neutral, and then dried at 100°C. In order to calculate the yield of NC-1 from NC-2, these two samples were weighed by analytical balance and the yield was then calculated to be 58.3% and 37.6%, respectively.

2.3. Characterization

X-ray diffraction (XRD) patterns were obtained on a Bruker D8 Advance X-ray diffractometer with Cu Kα radiation (λ = 1.54178 Å). Scanning electron microscopy (SEM) was performed on a LEO 1450VP scanning electron microscope. Transmission electron microscopy (TEM) was carried on a JEOL JEM-2010 electron microscope operating at 200 kV. Brunauer–Emmett–Teller (BET) surface area measurement was carried out using an ASAP 2020 porosimetry system (Micromeritics, USA). Fourier transform infrared spectroscopy (FTIR) spectra were obtained on a PerkinElmer Spectrum 100 spectrometer with samples embedded in KBr pellets.

2.4. Batch adsorption procedure

Batch adsorption was carried out in order to evaluate the adsorption capacity of the as-prepared CNFs. MB was selected as the representative of anionic dyes to probe the adsorption performance of the two samples. All batch adsorption experiments were carried out as follows: 50 mL of MB solutions with a various concentration and 20 mg of samples were added into 100 mL conical beaker. Subsequently, the conical beaker was shaken by the oscillator (SHZ-82, Changzhou Guohua Experimental Instrument Factory, China) at a speed of 150 rpm. After centrifugation, the solution absorbance was measured using visible light spectroscopy (721, Candy Precision Scientific Instrument Co., Ltd., China) at 668 nm. The amount of adsorbed dye on adsorbent (q_t, mg g^{-1}) at time t was calculated according to the following equation:

$$q_t = \frac{(C_0 - C_t)V}{m} \tag{1}$$

where C_0 is the initial concentration of dyes in solution (mg L^{-1}), C_t is the dyes concentration (mg L^{-1}) at time t, m is the mass of adsorbent (g) and V is the volume of solution (L).

The adsorption isotherms for MB were established by batch adsorption experiments. 20 mg CNFs were dispersed into 50 mL MB solutions with different concentration (20–200 mg L^{-1}). The adsorption was carried out at certain temperature (298–318 K) with constant shaking, and then kept for 12 h to establish adsorption equilibrium. The equilibrium adsorption capacity was determined using the following equation:

$$q_e = \frac{(C_0 - C_e)V}{m} \tag{2}$$

where C_0 is the initial concentration of MB solution (mg L^{-1}), C_e is the equilibrium concentration (mg L^{-1}), q_e is the equilibrium adsorption capacity (mg L^{-1}), m is the mass of adsorbent (g) and V is the volume of solution (L).

3. Results and discussion

3.1. Characterization of the as-prepared nanofibers

3.1.1. FTIR characterization of the Ni-NTA precursor and carbon nanofibers

The infrared (IR) spectra of the nanofiber precursor are shown in Fig. 1(a). The peak centered at 3,496.3 cm^{-1} can be ascribed to the –OH stretching frequencies, which caused by the adsorption of water molecule on the precursor sample. The appearance of carboxyl bands at 1,582.1 and 1,647.4 cm^{-1} can be assigned to the formation of –COONi coordination groups. NTA was a tetradentate ligand composed of three carbonyl groups and one amino group in the molecule structure, which had strong complexing tendency with metal cation. On the other hand, NTA was not soluble in water at room temperature. Under solvothermal condition of higher temperature, the gradually dissolved NTA began to complex with the Ni^{2+}. Ni-NTA coordination compound can be produced during the subsequent crystalline process. Isopropyl

alcohol due to the formation of microheterogeneities just like microemulsion in the mixed solvent may responsible for the growth of one-dimensional nanostructure with the polymer chains [29]. Therefore, long fiber-like products with light blue color were formed.

The two samples (NC-1 and NC-2) were obtained from the as-prepared Ni-NTA precursor nanofibers in two different methods. NC-1 was prepared through the sealing calcination of the Ni-NTA precursor, and NC-2 was obtained by treating the sample NC-1 with acid solution to remove the inorganic component. The FTIR spectra of these two samples were shown in Fig. 1(b). The two IR spectra displayed broadband at 3,375 cm^{-1}, which was associated with the stretching vibrations of hydrogen-bonded surface water molecules and hydroxyl groups. The bands around 2,922 and 1,402 cm^{-1} were corresponded to the C–H vibrations and C–O vibrations, respectively [30]. In the spectra of NC-1, the peak at 1,580 cm^{-1} was assigned to the stretching vibration of the carbonited C=C [31]. As to the NC-2, the bands at 1,618 cm^{-1} was attributed to the overlap of the carbonited C=C and the C=O stretching of carboxylic/carbonyl functional groups with relatively higher intensity [32]. Furthermore, the band at 1,256 cm^{-1} implied the existence of large numbers of residual

–O–C– in the spectrum of NC-1. However, the band became weak or disappeared in the spectrum of NC-2, indicating that the removal of inorganic component from the carbon fiber composite through the acid leaching.

3.1.2. SEM characterization of the as-prepared precursor and carbon nanofibers

The hydrothermal products of the precursor were observed by SEM. As shown in Fig. 2(a), lots of fibers with tens of micron were formed under hydrothermal condition. No other morphologies can be observed. Moreover, the morphology and structure of samples NC-1 and NC-2 were also analyzed by SEM. Low magnification SEM images of samples NC-1 and NC-2 are shown in Figs. 2(b) and (c), respectively. In Fig. 2(b), sample NC-1 almost maintained the long fiber-like morphology with high aspect ratio after sintering under sealed condition. No breakage or deformation was occurred. In Fig. 2(c), it can be seen that NC-2 also showed the fiber-like morphology and no obvious change can be observed after the
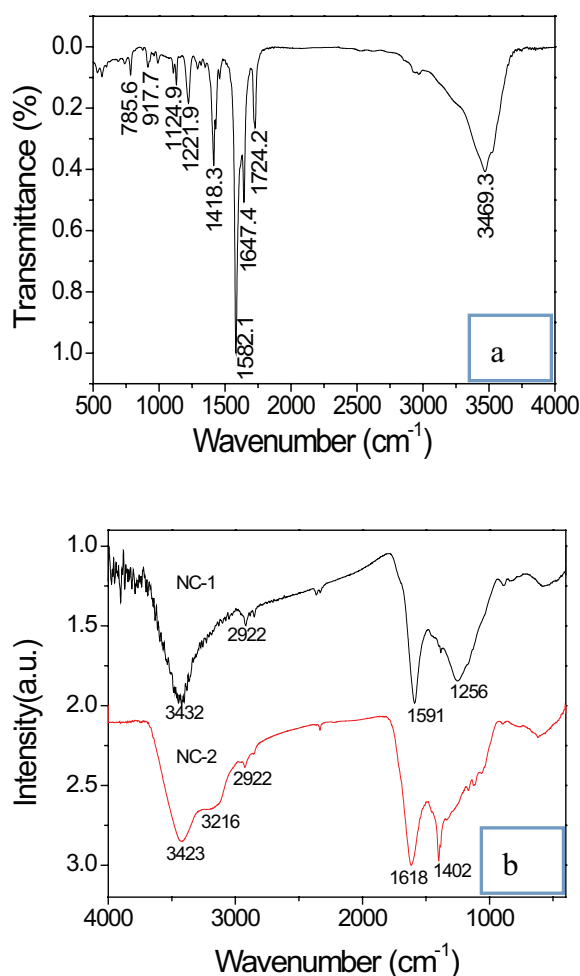

Fig. 1. FTIR spectra of the precursor nanofibers (a), samples NC-1 and NC-2 (b).
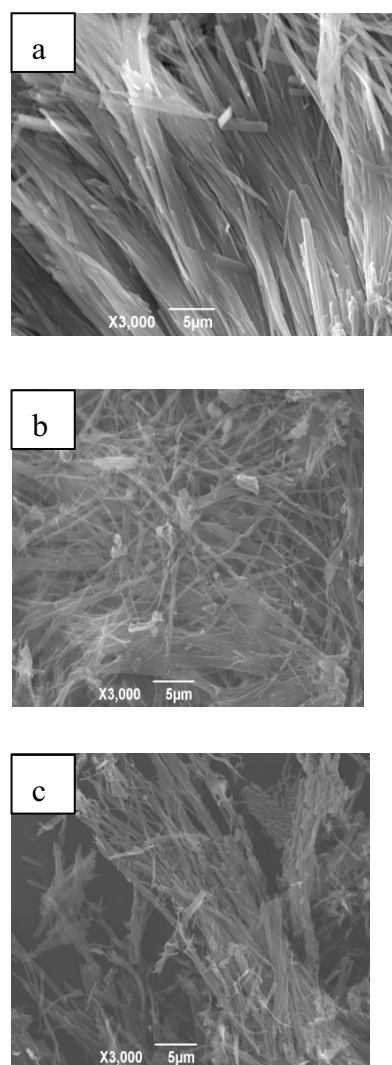

Fig. 2. SEM images of Ni-NTA precursor nanofiber (a), sample NC-1 (b) and sample NC-2 (c).

NC-1 sample was treated with acid leaching. By comparison with Ni-NTA nanofiber precursor, fibers products of samples NC-1 and NC-2 showed better dispersity.

3.1.3. XRD characterization of the as-prepared carbon nanofibers

The XRD patterns of NC-1 and NC-2 samples are shown in Fig. 3. In Fig. 3(a), the diffraction peaks at 44.5°, 51.8° and 76.4° could be attributed to the (111), (200) and (220) planes of cubic Ni (JCPDS no. 04-0850). Two diffraction peaks at 37.2° and 63.5° corresponded to the (111) and (222) reflections of NiO (JCPDS no. 078-1970) and the weak peak at 26.4° can be ascribed to graphite phase. The content of graphitic planes in the carbon materials was low due to the weak peak intensity and wide diffraction peaks [33]. The XRD result confirmed that the obtained NC-1 sample would be the composites of Ni, NiO and carbon. The content of NiO was much lower than that of Ni deduced from the intensity difference of their diffraction peaks. In Fig. 3(b), two obvious peaks at 26.38° and 44.39° could be attributed to the (002) and (101) diffractions of the graphite structure, indicating that a short-range order crystal structure existed in the obtained carbon material [34]. In addition, no other diffraction peak can be detected. The diffraction peaks of the Ni(NiO) particles disappeared in sample NC-2 through treatment of acid leaching (Fig. 3(c)), indicating the effective removal of the Ni(NiO) nanoparticles form the composite.

3.1.4. TEM characterization of the as-prepared precursor and carbon nanofibers

Microstructure of the as-prepared precursor and samples was investigated by TEM images as shown in Fig. 4. In Fig. 4(a), the as-prepared Ni-NTA precursor nanofiber had smooth surface and the diameter of the fibers was about 100 nm. In addition, the fiber shape of Ni-NTA as self-sacrificial templates can be well maintained in the carbonization product after the heat treatment (Fig. 4(b)). More importantly, we found that the carbonized fibers were constructed by plenty of nanoparticles with the average diameter in 10 nm as
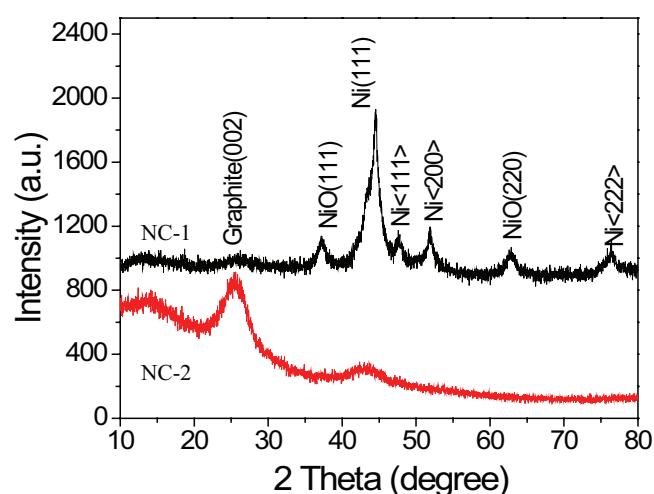
observed from Fig. 4(c). The worm-like area was recognized as the holes which were built among lots of nanoparticles. Furthermore, the disordered carbon layer was coated on the surface of nanoparticles as also observed. The fibrous structure with average diameter of 200 nm still was retained even after the treatment of hydrochloric acid and the nanoparticles as the basic building block can also be observed in the image (Fig. 4(d)). Further observation showed that these particles were hollow nanosphere with the diameter of 10 nm as shown in Fig. 4(e). Therefore, the NC-2 sample was the nanofibers constructed by hollow carbon nanosphere. The formation of hollow structure can be ascribed to the removal of Ni(NiO) in the fiber composite.
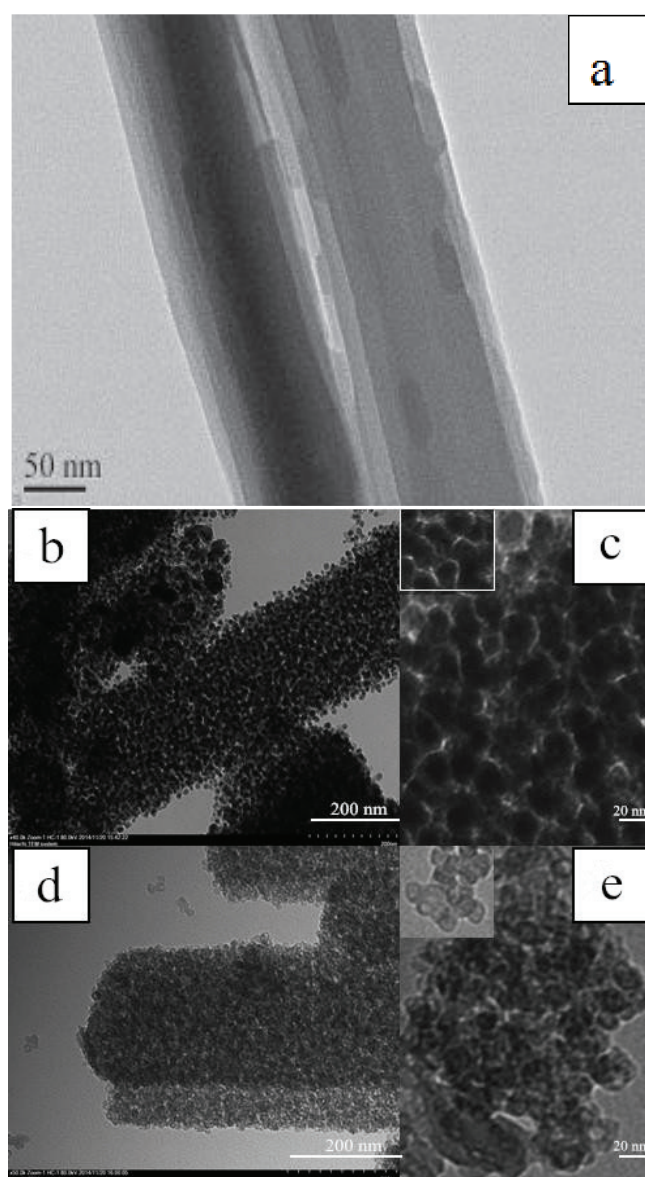

Fig. 4. TEM images of Ni-NTA precursor nanofiber (a), sample NC-1 (b) and (c) and sample NC-2 (d) and (e) with different magnification view (the scale bar of (b) and (d) is 200 nm, respectively; the scale bar of (c) and (e) is 20 nm, respectively).

Fig. 3. XRD patterns of samples NC-1 and NC-2.

3.1.5. BET measurement of the as-prepared carbon nanofibers

The pore texture properties of samples NC-1 and NC-2 were further evaluated by nitrogen adsorption and desorption measurements and the obtained results are illustrated in Fig. 5. As shown in Fig. 5(a), the N_2 sorption isotherms of NC-2 sample exhibited representative type IV curves with a distinct H3-type hysteresis loop over the relative pressure range 0.4–1.0, resulting from the assemblages of slit-shaped pores. The BET specific surface area and the total pore volume of NC-2 sample were 291.4 m^2 g^{-1} and 0.822 cm^3 g^{-1}, respectively. The pore-size distribution calculated by the Barrett–Joyner–Halenda (BJH) method based on the desorption branch of the isotherms indicated a mesopore size of 12.8 nm in addition to a distribution determined at 4 nm (Fig. 5(b)). The porous structure of the composite fibers can be attributed to the thermal decomposition of Ni-NTA, where the many oxygen-containing groups (–OH and –COOH) convert to H_2O and CO_2 during the heat treatment. Compared with those of NC-2 sample,
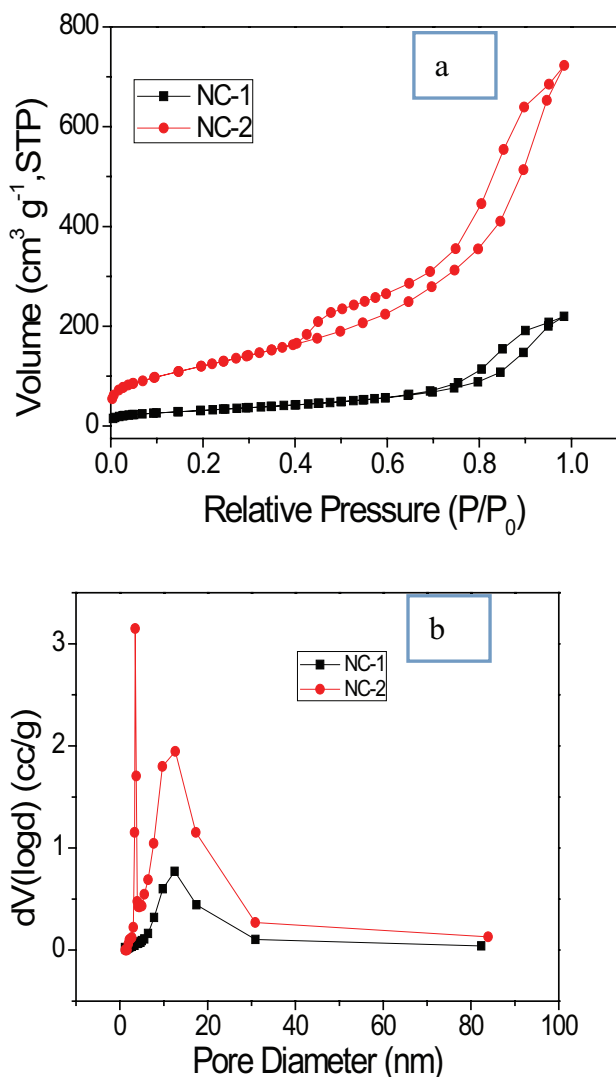
the sorption isotherms and pore-size distribution curves of NC-1 sample displayed type IV curves with a hysteresis loop at relatively high pressure of $P/P_0 = 0.75–1.0$, which confirmed the existence of pore structure. The BET surface area of NC-1 sample was 53 m^2 g^{-1} calculated from N_2 isotherms at 77 K and pore distribution with an average diameter of 3.8 nm can be estimated by the BJH method, indicating a lower BET-specific surface area (144.4 m^2 g^{-1}), a smaller total pore volume (0.356 cm^3 g^{-1}) and mesopore size (12.5 nm). The increase of pore structure parameter (~4 nm) of NC-2 sample was attributed to the removal of Ni and NiO component formed during the sealed calcination process.

3.1.6. Formation mechanism analysis of the as-prepared carbon nanofibers

According to the results of XRD, SEM and TEM analyses of the samples, the formation mechanism of the porous carbon fibers built by hollow carbon nanoparticles is illustrated in Fig. 6. Ni-NTA coordination nanofibers were first formed after the hydrothermal treatment of Ni^{2+} and NTA with the mixture of isopropanol and water. Under the sealed heat treatment, Ni-NTA coordination nanofibers were in situ decomposed into the composite constructed by Ni/NiO nanosphere coated with carbon layer while maintaining the fiber-like morphology. The porous CNFs assembled by hollow carbon nanospheres can be formed after the removal of Ni/NiO core of nanospheres. The specific area of the nanofibers would be accordingly increased due to the hollowing of the nanosphere unit, which was further testified by subsequent BET measurement.

3.2. Adsorption performance

3.2.1. Effect of pH

The pH of solution is another important influencing factor for dye adsorption as it directly affects the dissociative and adsorptive ability of the dye on the adsorbent surface. For MB the pH range was chosen as 4–10 for NC-1 and NC-2. The pH of the test solutions was adjusted by using HCl and NaOH solutions. As depicted in Fig. 7, it was observed that the removal rate of MB increased when pH varied from 4 to 10 and the increasing tendency became slow when pH is higher than 7 for NC-1 and NC-2 adsorbents. This may be attributed

Fig. 5. Nitrogen adsorption–desorption isotherm and BJH pore-size distribution plot of samples NC-1 and NC-2.
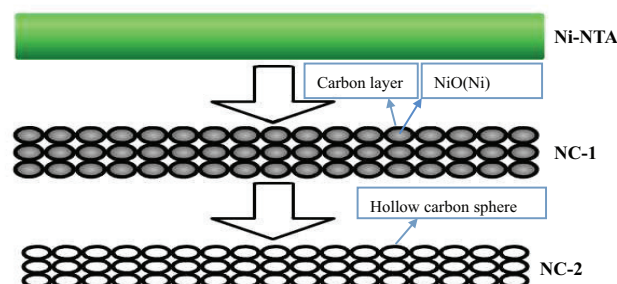

Fig. 6. Schematic illustration of the synthesis procedure of porous carbon nanofibers.

to the contributions of as-prepared nanofibers adsorption toward MB molecules resulted from electrostatic attraction between the negatively charged adsorbent surface and the positively charged cationic MB molecules. In order to ascertain the practical applicability of the adsorption of this dye, pH 7 (neutral water) was chosen for the further experiments.

3.2.2. Effect of adsorption time

In order to investigate the remediation performance of the as-prepared nanofibers for the dye wastewater, MB was employed as a model to examine the adsorption property. The effect of adsorption time on the adsorption capacity of NC-1 and NC-2 samples for MB is shown in Fig. 8. The results indicated that the adsorption capacity of NC-1 and NC-2 samples for MB increased with an increase in adsorption time until equilibrium was reached between the adsorbents and dye solution. It can be seen that there was a rapid uptake of NC-2 sample for MB. The adsorption can reach equilibrium time within 30 min. However, the adsorption for MB onto NC-1 sample was much slower and the equilibrium time was about 400 min. Furthermore, the equilibrium capacity (20 mg g^{-1}) was much lower than that of NC-2 sample (120 mg g^{-1}). Higher equilibrium capacity and shorter equilibrium time of MB onto sample NC-2 than that o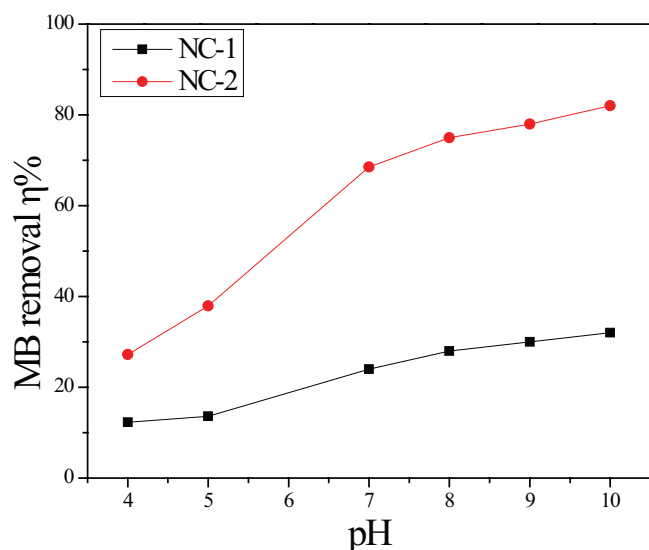f sample NC-1 can be ascribed to the increase of surface area due to the removal of Ni(NiO) core from the composite nanoparticles.

3.2.3. Adsorption kinetics

It is well known that the Lagergren rate equation is one of the most widely used adsorption rate equations for the adsorption of solute from a liquid solution. In order to acquire information about the mechanism of MB adsorption onto NC-1 and NC-2 samples, the adsorption kinetics was investigated with the help of three kinetic models, namely the Lagergren pseudo-first-order model and Lagergren pseudo-second-order model [35,36]. The referred models can be expressed by the following equations:

$$\ln(Q_e - Q_t) = \ln Q_e - K_1 t \tag{3}$$

$$\frac{t}{Q_t} = \frac{1}{K_2 Q_e^2} + \frac{t}{Q_e} \tag{4}$$

where Q_e and Q_t are the amount adsorbed at equilibrium at any time t (mg g^{-1}), K_1 and K_2 are the constant of adsorption for the Lagergren pseudo-first-order model and Lagergren pseudo-second-order model, respectively.

Both equations were used to correlate the adsorption kinetic data through linear regressions. The linear plots are shown in Fig. 8. The corresponding model parameters derived from the plot results are summarized in Table 1. The values of experimental Q_e of NC-1 and NC-2 did not agree with the calculated ones obtained from the linear plots by

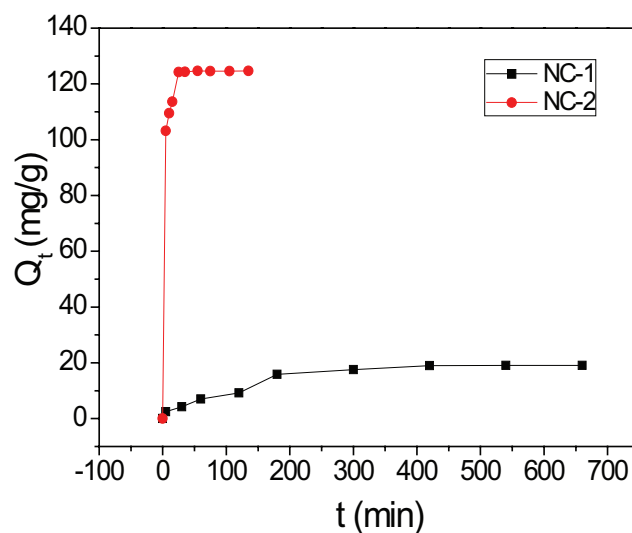Fig. 7. Effect of pH on the adsorption of MB of samples NC-1 and NC-2.

Fig. 8. Effect of time on the adsorption of MB of samples NC-1 and NC-2 (initial MB solution concentration: 50 mg L^{-1}; pH: 7.0; adsorption temperature: 25°C ± 2°C).

Table 1
Pseudo-first-order and pseudo-second-order kinetics model parameters for MB adsorption onto samples NC-1 and NC-2

Sample	Pseudo-first-order			Pseudo-second-order			
	K_1 (min^{-1})	$q_{e,\text{cal}}$ (mg g^{-1})	R^2	K_2 (g mg^{-1} min^{-1})	$q_{e,\text{cal}}$ (mg g^{-1})	$q_{e,\text{exp}}$ (mg g^{-1})	R^2
NC-1	0.0166	33.96	0.9127	0.0004	22.68	19.11	0.9686
NC-2	0.0747	20.56	0.7843	0.0082	126.58	124.63	0.9998

Lagergren pseudo-first-order model and the values of correlation coefficient (R^2) were relatively low for most of the adsorption data. On the contrary, the linear plots of t/Q_t vs. t by Lagergren pseudo-second-order model showed good agreement between experimental and calculated Q_e values of NC-1 and NC-2. The correlation coefficient (R^2) for the pseudo-second-order adsorption model had high value for adsorbent (Table 1). These results suggested that the pseudo-second-order adsorption mechanism can well describe the adsorption process of MB onto NC-1 and NC-2.

The steps of adsorption process were identified by the intra-particle diffusion model as proposed by Weber and Morris [37]. The model can be expressed as follow:

$$q_t = k_p t^{0.5} + C \tag{5}$$

where k_p is the intra-particle diffusion rate constant (mmol g^{-1} h$^{0.5}$) and C is a constant.

According to this model, the plot of Q_t vs. $t^{0.5}$ must be a straight line with a slope k_{id} and the intercept C. Fig. 9 presents a linear fit of intra-particle diffusion model for adsorption of MB onto NC-1 and NC-2. The plots of q_t vs. $t^{0.5}$ do not pass through the origin, indicating that the rate-limiting process was not only the intra-particle diffusion. The multi-linearity correlation indicated that two or more steps occurred during the adsorption process. The initial region was a diffusion adsorption stage, attributing to the diffusion of dye through the solution to the external surface of adsorbent (external diffusion). The second region was a gradual adsorption stage, corresponding to intra-particle diffusion of dye molecules through the pores of adsorbent (intra-particle diffusion). The parameters and R^2 of intra-particle diffusion model are shown in Table 2. It can be easily observed that k_{i1} was larger than k_{i2} for both NC-1 and NC-2, indicating film diffusion was a rapid process while intra-particle diffusion was a gradual process. Furthermore, the value of k_{i1} and k_{i2} with sample NC-2 was larger than that with sample NC-1, which can be ascribe to a larger surface area and pore volume of NC-2 for solute adsorption instantaneously.

3.2.4. Adsorption isotherms

The equilibrium adsorption models can provide a number of useful information including adsorption capacity, surface properties of adsorbent and affinity of the adsorbent [38]. As we know, Langmuir and Freundlich models were the two typical adsorption isotherm models for describing adsorption of dyes from aqueous solution [39,40]. The two models were used to correlate the adsorption behavior in present study. Linearized Langmuir and Freundlich isotherm models were presented by the following equations:

$$\frac{C_e}{Q_e} = \frac{1}{Q_m K_L} + \frac{C_e}{Q_m} \tag{6}$$

$$\ln Q_e = \ln K_F \frac{\ln C_e}{n} \tag{7}$$

where Q_m (mg g^{-1}) is the maximum adsorption capacity, K_L (L mg^{-1}) is the Langmuir constant related to the energy of
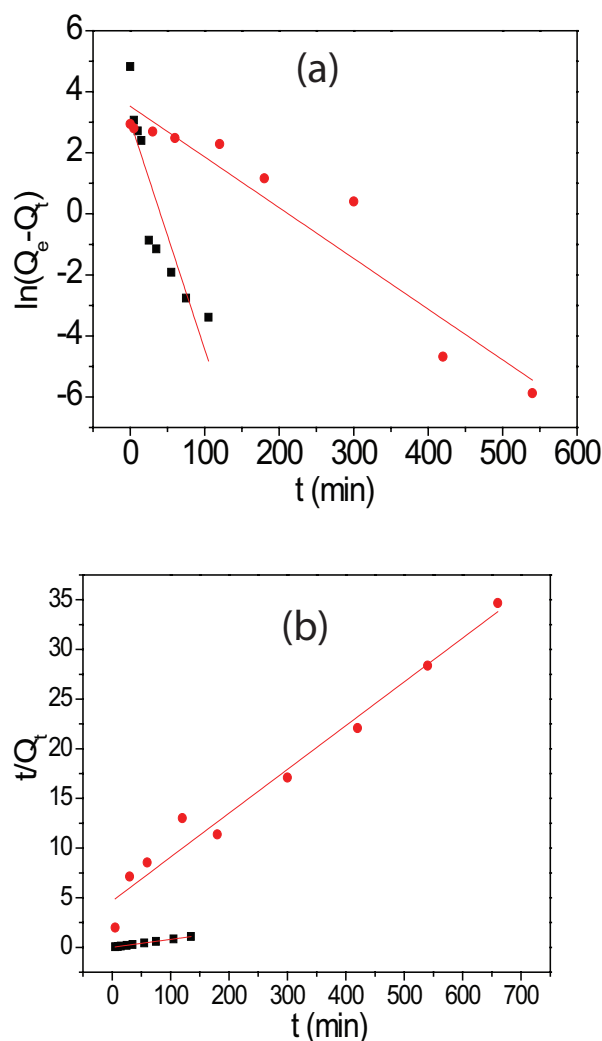

Fig. 9. Plots of the pseudo-first-order (a) and pseudo-second-order kinetics (b) related to the adsorption of MB adsorption onto samples NC-1 and NC-2.

Table 2
Intra-particle diffusion model parameters for MB adsorption onto samples NC-1 and NC-2

Sample	Intra-particle diffusion model					
	k_{i1} (mg g^{-1} min$^{-0.5}$)	C_{i1} (mg g^{-1})	R^2	k_{i2} (mg g^{-1} min$^{-0.5}$)	C_{i2} (mg g^{-1})	R^2
NC-1	1.0356	0.8059	0.9704	0.0018	18.9926	0.9261
NC-2	7.5376	85.7130	0.9823	0.0558	123.908	0.9963

adsorption, K_F and $1/n$ constants are related to the adsorption capacity and intensity of adsorption.

Adsorption isotherms of MB onto NC-1 and NC-2 samples were performed between 298 and 318 K. The adsorption isotherms of MB removal by nanofiber at temperature of 298, 308 and 318 K are shown in Fig. 10. It can be seen that there was an increase of the adsorption capacity with an increase of solution temperature, indicating that MB adsorption by the nanofiber was endothermic in nature. The Langmuir and Freundlich constants can be obtained by linear regression analysis as shown in Fig. 11. Table 3 presents the results and the coefficient of determination (R^2). It can be seen that the R^2 values of Langmuir isotherm were greater than those for Freundlich isotherm, indicating that Langmuir model was better fitted the experimental data than Freundlich model at investigated temperatures. MB molecule was adsorbed onto the surface of NC-1 and NC-2 by the monolayer coverage of dye (Fig. 12). The dimensionless constant separation factor $\left(R_L = \frac{1}{1+bC_0}\right)$ as the essential characteristics of the Langmuir isotherm was calculated. Values of separation factor for both the adsorbents were found to be between 0 and 1, confirming that the adsorption process was favorable in both cases [41].

3.2.5. Thermodynamic parameters of adsorption

The thermodynamic parameters of standard Gibbs free energy change ($\Delta G°$), enthalpy change ($\Delta H°$) and entropy change ($\Delta S°$) associated with the adsorption process were calculated using the following equations [42,43]:

$$\Delta G° = -RT\ln(K_L) \tag{8}$$

$$\ln(K_L) = \frac{\Delta S°}{R} - \frac{\Delta H°}{RT} \tag{9}$$

Fig. 11. Adsorption isotherms of MB onto sample NC-1 (a) and sample NC-2 (b) at various temperatures.
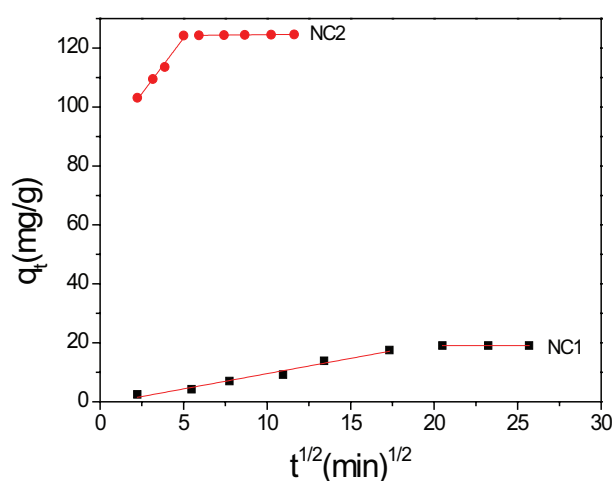

Fig. 10. Plots of intra-particle diffusion model related to the adsorption of MB onto samples NC-1 and NC-2.

Table 3
Isotherm parameters for MB adsorption onto samples NC-1 and NC-2

Sample	Temperature (K)	Langmuir constants			Freundlich constants		
		Q_m (mg g^{-1})	K_L (L mg^{-1})	R^2	K_F (mg g^{-1})	N (L mg^{-1})	R^2
NC-1	298	31.63	0.1755	0.9894	7.9615	2.8968	0.9270
	308	34.35	0.3016	0.9984	12.5153	3.8149	0.9431
	318	36.94	0.3983	0.9964	15.2807	4.2674	0.9624
NC-2	298	144.93	0.0563	0.9849	39.3013	4.1278	0.9524
	308	154.08	0.0607	0.9803	42.5908	4.1404	0.9429
	318	157.48	0.0834	0.9941	45.9447	4.1540	0.9653

where K_L is the Langmuir equilibrium constant (L mol^{-1}), R (J mol^{-1} K^{-1}) is the gas constant and T (K) is the absolute solution temperature. $\Delta G°$ can be calculated according to equation. The values of $\Delta H°$ and $\Delta S°$ were obtained from the slope and intercept of the plot of lnK_L vs. $1/T$.

The values of $\Delta G°$, $\Delta H°$ and $\Delta S°$ of MB adsorption onto samples NC-1 and NC-2 are presented in Table 4. From the

Table 4
Thermodynamic data for the adsorption of MB on samples NC-1 and NC-2

Sample	Temperature (K)	$\Delta G°$ (kJ mol^{-1})	$\Delta H°$ (kJ mol^{-1})	$\Delta S°$ (J mol^{-1} K^{-1})
NC-1	298	−37.06	32.39	233.3
	308	−39.69		
	318	−41.72		
NC-2	298	−34.24	15.38	166.1
	308	−35.59		
	318	−37.58		

plot, both the change in entropy ($\Delta S°$) and enthalpy ($\Delta H°$) of MB adsorption onto sample NC-1 were determined and are 0.2333 J mol^{-1} K^{-1} and 34.39 kJ mol^{-1}, respectively. Similarly, the change in entropy ($\Delta S°$) and the enthalpy ($\Delta H°$) of MB adsorption onto sample NC-1 were 0.1661 J mol^{-1} K^{-1} and 15.38 kJ mol^{-1}, respectively. The negative values of $\Delta G°$ supported the spontaneity of the process of adsorption. The positive value of $\Delta H°$ suggested the endothermic nature of adsorption for MB, which was consistent with the isotherm study. The positive value of $\Delta S°$ showed the randomness was slightly increased at the adsorbent/solution interface during the adsorption of MB onto NC-1 and NC-2.

4. Conclusions

In this study, porous CNFs were successfully prepared by sealed thermal treatment of Ni-NTA with subsequent acid leaching. Ni-NTA nanofibers were synthesized by hydrothermal method. The as-synthesized porous CNFs were built by plenty of hollow carbon spheres and had more amount of –COOH groups left on the surface, which can be
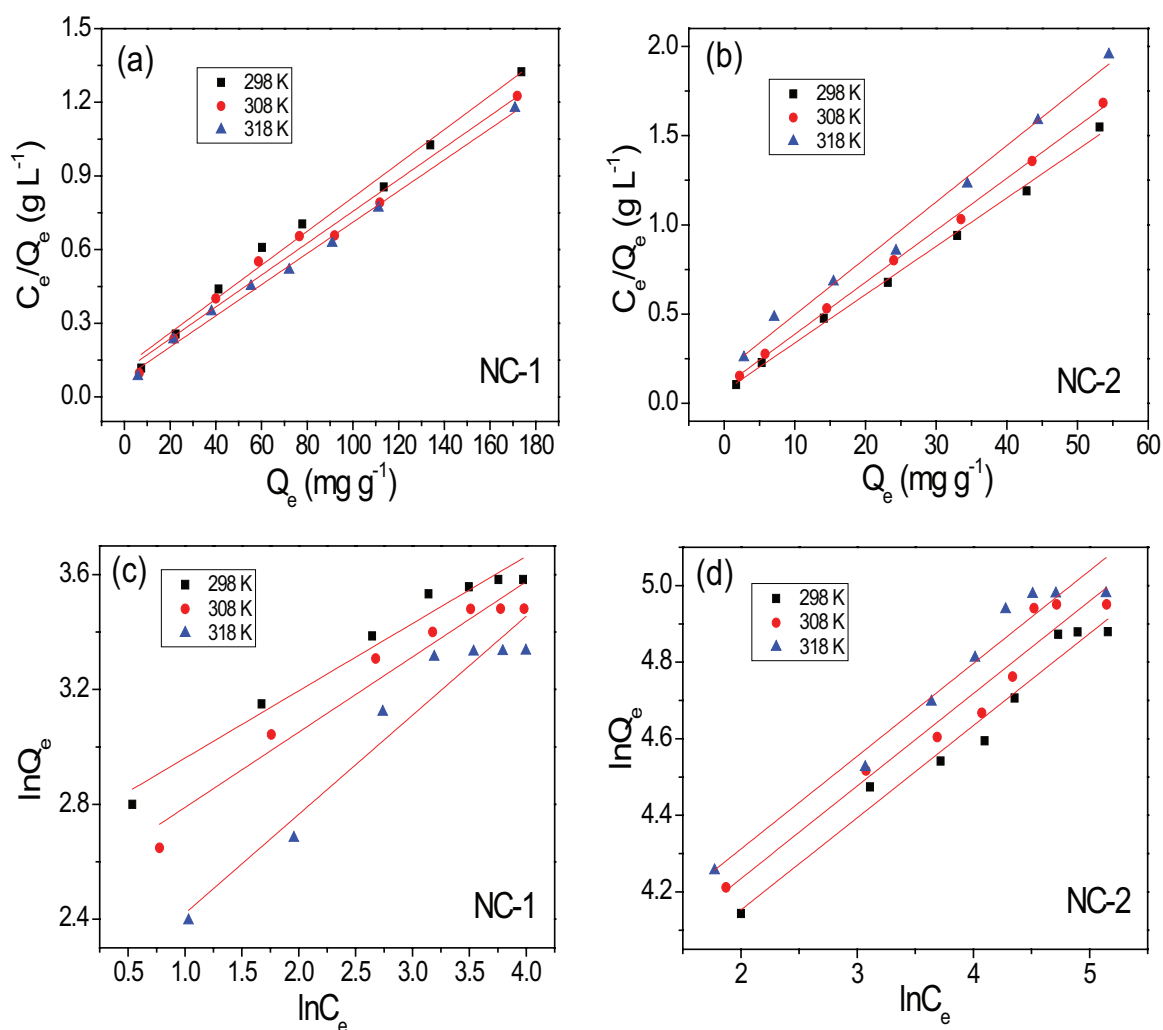

Fig. 12. Langmuir and Freundlich plots for the adsorption of MB onto sample NC-1 (a) and (c) and sample NC-2 (b) and (d) at various temperatures.

effectively adsorb cationic dyes. Moreover, the surface area of CNFs can be further enlarged by the removal of the in situ formed Ni(NiO) nanoparticles. These characteristic of CNFs endowed them to be the excellent absorbent for the removal of MB from aqueous solution. Thermodynamic and kinetics study of MB adsorption onto the as-prepared CNFs were systematically conducted. Results showed that the pseudo-second-order kinetic model could better describe adsorption kinetics of MB adsorption onto the two CNFs, and the adsorption of MB onto the two CNFs was monolayer adsorption and followed the Langmuir isotherm. The values of thermodynamic parameters ($\Delta G°$, $\Delta H°$ and $\Delta S°$) suggested that MB adsorption onto the two CNFs were endothermic and spontaneous. Higher temperature was favorable for the increase of adsorption capacity. This study developed a novel route to prepare porous CNFs with rich carboxyl groups, and these carbon materials can be employed efficient adsorbent for the removal of dyes from aqueous solution.

References

[1] M. Anbia, S. Salehi, Enriched graphitic N-doped carbon-supported Fe_3O_4 nanoparticles as efficient electrocatalysts for oxygen reduction reaction, Dyes Pigm., 94 (2012) 1–9.

[2] A.A. Kadam, H.S. Lade, S.M. Patil, S.P. Govindwar, Low cost $CaCl_2$ pretreatment of sugarcane bagasse for enhancement of textile dyes adsorption and subsequent biodegradation of adsorbed dyes under solid state fermentation, Bioresour. Technol., 132 (2013) 276–284.

[3] Y.Q. Hu, T. Guo, X.S. Ye, Q. Li, M. Guo, H.N. Liu, Z.J. Wu, Dye adsorption by resins: effect of ionic strength on hydrophobic and electrostatic interactions, Chem. Eng. J., 228 (2013) 392–397.

[4] I.E. Saliby, L. Erdei, J.H. Kim, H.K. Shon, Adsorption and photocatalytic degradation of methylene blue over hydrogen–titanate nanofibres produced by a peroxide method, Water Res., 47 (2013) 4115–4125.

[5] A.M. Ferreira, J.A.P. Coutinho, A.M. Fernandes, M.G. Freire, Complete removal of textile dyes from aqueous media using ionic-liquid-based aqueous two-phase systems, Sep. Purif. Technol., 128 (2014) 58–66.

[6] M.S. álvarez, F. Moscoso, A. Rodríguez, M.A. Sanromán, F.J. Deive, Novel physico-biological treatment for the remediation of textile dyes-containing industrial effluents, Bioresour. Technol., 146 (2013) 689–695.

[7] H. Wang, X.W. Zheng, J.Q. Su, Y. Tian, X.J. Xiong, T.L. Zheng, Biological decolorization of the reactive dyes Reactive Black 5 by a novel isolated bacterial strain *Enterobacter* sp. EC3, J. Hazard. Mater., 171 (2009) 654–659.

[8] M.E. Osugi, K. Rajeshwar, E.R.A. Ferraz, D.P. Oliveira, Â.R. Araújo, M.V.B. Zanoni, Comparison of oxidation efficiency of disperse dyes by chemical and photoelectrocatalytic chlorination and removal of mutagenic activity, Electrochim. Acta, 54 (2009) 2086–2093.

[9] Y. Zhang, D.L. Li, Y. Chen, X.H. Wang, S.T. Wang, Catalytic wet air oxidation of dye pollutants by polyoxomolybdate nanotubes under room condition, Appl. Catal., B, 86 (2009) 182–189.

[10] M. Punzi, A. Anbalagan, R.A. Börner, B.M. Svensson, M. Jonstrup, B. Mattiasson, Degradation of a textile azo dye using biological treatment followed by photo-Fenton oxidation: evaluation of toxicity and microbial community structure, Chem. Eng. J., 270 (2015) 290–299.

[11] K.K. Panda, A.P. Mathews, Ozone oxidation kinetics of Reactive Blue 19 anthraquinone dye in a tubular in situ ozone generator and reactor: modeling and sensitivity analyses, Chem. Eng. J., 255 (2014) 553–567.

[12] X.J. Zhou, W.Q. Guo, S.S. Yang, H.S. Zheng, N.Q. Ren, Ultrasonic-assisted ozone oxidation process of triphenylmethane dye degradation: evidence for the promotion effects of ultrasonic on malachite green decolorization and degradation mechanism, Bioresour. Technol., 128 (2013) 827–830.

[13] T. Sreethawong, S. Ngamsinlapasathian, S. Yoshikawa, Photochemically deposited nano-Ag/sol–gel TiO_2–In_2O_3 mixed oxide mesoporous-assembled nanocrystals for photocatalytic dye degradation, J. Colloid Interface Sci., 421 (2014) 191–198.

[14] V. Vaiano, O. Sacco, D. Sannino, P. Ciambelli, Nanostructured N-doped TiO_2 coated on glass spheres for the photocatalytic removal of organic dyes under UV or visible light irradiation, Appl. Catal., B, 170–171 (2015) 153–161.

[15] Y.Y. Lau, Y.S. Wong, T.T. Teng, N. Morad, M. Rafatullah, S.A. Ong, Coagulation-flocculation of azo dye Acid Orange 7 with green refined laterite soil, Chem. Eng. J., 246 (2014) 383–390.

[16] S. Liu, Q.H. Wang, H.Z. Ma, P.K. Huang, J. Li, T. Kikuchi, Effect of micro-bubbles on coagulation flotation process of dyeing wastewater, Sep. Purif. Technol., 71 (2010) 337–346.

[17] C. Yang, L. Li, J.L. Shi, C. Long, A.M. Li, Advanced treatment of textile dyeing secondary effluent using magnetic anion exchange resin and its effect on organic fouling in subsequent RO membrane, J. Hazard. Mater., 284 (2015) 50–57.

[18] M. Wawrzkiewicz, Basic Blue 3 dye by sorption onto cation exchange resin, functionalized and non-functionalized polymeric sorbents from aqueous solutions and wastewaters, Chem. Eng. J., 217 (2013) 414–425.

[19] G. Durán-Jiménez, V. Hernández-Montoya, M.A. Montes-Morán, A. Bonilla-Petriciolet, N.A. Rangel-Vázquez, Adsorption of dyes with different molecular properties on activated carbons prepared from lignocellulosic wastes by Taguchi method, Microporous Mesoporous Mater., 199 (2014) 99–107.

[20] W.S.W. Ngah, L.C. Teong, M.A.K.M. Hanafiah, Adsorption of dyes and heavy metal ions by chitosan composites: a review, Carbohydr. Polym., 83 (2011) 1446–1456.

[21] M.M. Teng, J.L. Qiao, F.T. Li, P.K. Bera, Electrospun mesoporous carbon nanofibers produced from phenolic resin and their use in the adsorption of large dye molecules, Carbon, 50 (2012) 2877–2886.

[22] A. Chakraborty, D. Deva, A. Sharma, N. Verma, Adsorbents based on carbon microfibers and carbon nanofibers for the removal of phenol and lead from water, J. Colloid Interface Sci., 359 (2011) 228–239.

[23] Y.Y. Sun, G. Wang, Q. Dong, B.Q. Qian, Y.L. Meng, J.S. Qiu, Electrolysis removal of methyl orange dye from water by electrospun activated carbon fibers modified with carbon nanotubes, Chem. Eng. J., 253 (2014) 73–77.

[24] T.H. Le, Y. Yang, Z.H. Huang, F.Y. Kang, Preparation of microporous carbon nanofibers from polyimide by using polyvinyl pyrrolidone as template and their capacitive performance, J. Power Sources, 278 (2015) 683–692.

[25] A. Simon, M. Seyring, S. Kämnitz, H. Richter, I. Voigt, M. Rettenmayr, U. Ritter, Carbon nanotubes and carbon nanofibers fabricated on tubular porous Al_2O_3 substrates, Carbon, 90 (2015) 25–33.

[26] C.J. Wang, T.C. Chen, J.H. Lin, P.R. Huang, H.J. Tsai, C.S. Chen, One-step preparation of hydrophilic carbon nanofiber containing magnetic Ni nanoparticles materials and their application in drug delivery, J. Colloid Interface Sci., 440 (2015) 179–188.

[27] H.Y. Wang, J.J. Moore, Low temperature growth mechanisms of vertically aligned carbon nanofibers and nanotubes by radio frequency-plasma enhanced chemical vapor deposition, Carbon, 50 (2012) 1235–1242.

[28] G.X. Wang, X.L. Gou, J. Horvat, J. Park, Facile synthesis and characterization of iron oxide semiconductor nanowires for gas sensing application, J. Phys. Chem. C, 112 (2008) 15220–15225.

[29] C.C. Li, X.M. Yin, L.B. Chen, Q.H. Li, T.H. Wang, Synthesis of cobalt ion-based coordination polymer nanowires and their conversion into porous Co_3O_4 nanowires with good lithium storage properties, Chem. Eur. J., 17 (2010) 5215–5221.

[30] Y.F. Zhao, W. Ran, J. He, Y.F. Song, C.M. Zhang, D.B. Xiong, F.M. Gao, J.S. Wu, Y.Y. Xia, Synthesis of uniform and superparamagnetic Fe_3O_4 nanocrystals embedded in a porous carbon matrix for a superior lithium ion battery anode, ACS Appl. Mater. Interfaces, 7 (2015) 1132–1139.

[31] B.K. Pradhan, N.K. Sandle, Enriched graphitic N-doped carbon-supported Fe_3O_4 nanoparticles as efficient electrocatalysts for oxygen reduction reaction, Carbon, 37 (1999) 1323.

[32] H.Y. Li, K. Jiao, L. Wang, C. Wei, X.L. Li, B. Xie, Oxygen-rich hierarchical porous carbon derived from artemia cyst shells with superior electrochemical performance, J. Mater. Chem. A, 2 (2014) 18806–18815.

[33] S. Wu, Z.Y. Wang, C.N. He, N.Q. Zhao, C.S. Shi, E.Z. Liu, J.J. Li, Effect of different oxidizing agent treatments on the surface properties of activated carbons, J. Mater. Chem. A, 1 (2013) 11011–11018.

[34] Y.H. Su, H.L. Jiang, Y.H. Zhu, X.L. Yang, J.H. Shen, W.J. Zou, J.D. Chen, C.Z. Li, Micelle anchored in situ synthesis of V_2O_3 nanoflakes@C composites for supercapacitors, J. Mater. Chem. A, 2 (2014) 7281–7287.

[35] O. Aksakal, H. Ucun, Equilibrium, kinetic and thermodynamic studies of the biosorption of textile dye (Reactive Red 195) onto *Pinus sylvestris* L, J. Hazard. Mater., 181 (2010) 666–672.

[36] G.Q. Xiao, R.M. Wen, D.M. Wei, D. Wu, Effects of the steric hindrance of micropores in the hyper-cross-linked polymeric adsorbent on the adsorption of *p*-nitroaniline in aqueous solution, J. Hazard. Mater., 280 (2014) 97–103.

[37] Q.T. Lin, J.X. Pan, Q.L. Lin, Q.J. Liu, Microwave synthesis and adsorption performance of a novel crosslinked starch microsphere, J. Hazard. Mater., 263 (2013) 517–524.

[38] J.T. Feng, J.W. Zhu, W. Lv, J.J. Li, W. Yan, Effect of hydroxyl group of carboxylic acids on the adsorption of Acid Red G and Methylene Blue on TiO_2, Chem. Eng. J., 269 (2015) 316–322.

[39] O.G. Apul, T. Karanfil, Adsorption of synthetic organic contaminants by carbon nanotubes: a critical review, Water Res., 68 (2015) 34–55.

[40] L.K. Ong, F.E. Soetaredjo, A. Kurniawan, A. Ayucitra, J.C. Liu, S. Ismadji, Investigation on the montmorillonite adsorption of biocidal compounds incorporating thermodynamical-based multicomponent adsorption isotherm, Chem. Eng. J., 241 (2014) 9–18.

[41] B. Ismail, S.T. Hussain, S. Akram, Adsorption of methylene blue onto spinel magnesium aluminate nanoparticles: adsorption isotherms, kinetic and thermodynamic studies, Chem. Eng. J., 219 (2013) 395–402.

[42] D.L. Guerra, W.L.L. Silva, H.C.P. Oliveira, R.R. Viana, C. Airoldi, Organofunctionalized Amazon smectite for dye removal from aqueous medium—kinetic and thermodynamic adsorption investigations, J. Hazard. Mater., 186 (2011) 675–682.

[43] J.S. Piccin, C.S. Gomes, L.A. Feris, M. Gutterres, Kinetics and isotherms of leather dye adsorption by tannery solid waste, Chem. Eng. J., 183 (2012) 30–38.